Monthly Notices of the ROYAL ASTRONOMICAL SOCIETY

MNRAS **516,** 3786–3801 (2022) https://doi.org/10.1093/mnras/stac2361
Advance Access publication 2022 August 25

Enrichment of the Galactic disc with neutron-capture elements: Gd, Dy, and Th

T. Mishenina,[1]★ M. Pignatari,[2,3,4,5]★† T. Gorbaneva,[1] B. Côté,[2,5,6]† A. Yagüe López,[2,7]† F.-K. Thielemann[8,9] and C. Soubiran[10]

[1]*Astronomical Observatory, Odessa National University, Shevchenko Park, 65014 Odessa, Ukraine*
[2]*Konkoly Observatory, Research Centre for Astronomy and Earth Sciences (CSFK), Eötvös Loránd Research Network (ELKH), Konkoly Thege Miklós út 15-17, H-1121 Budapest, Hungary*
[3]*CSFK, MTA Centre of Excellence, Budapest, Konkoly Thege Miklós út 15-17, H-1121 Budapest, Hungary*
[4]*Department of Physics and Mathematics, E.A. Milne Centre for Astrophysics, University of Hull, Hull HU6 7RX, UK*
[5]*Joint Institute for Nuclear Astrophysics – Center for the Evolution of the Elements, East Lansing, Michigan 48824, USA*
[6]*Department of Physics and Astronomy, University of Victoria, Victoria, BC V8P 5C2, Canada*
[7]*Computer, Computational and Statistical Sciences (CCS) Division, Center for Theoretical Astrophysics, Los Alamos National Laboratory, Los Alamos, NM 87545, USA*
[8]*Department of Physics, University of Basel, Klingelbergstrabe 82, CH-4056 Basel, Switzerland*
[9]*GSI Helmholtzzentrum für Schwerionenforschung, Planckstrasse 1, D-64291 Darmstadt, Germany*
[10]*Laboratoire d'Astrophysique de Bordeaux, Univ. Bordeaux – CNRS, B18N, allée Geoffroy Saint-Hilaire, F-33615 Pessac, France*

Accepted 2022 August 18. Received 2022 August 17; in original form 2022 March 2

ABSTRACT

The study of the origin of heavy elements is one of the main goals of nuclear astrophysics. In this paper, we present new observational data for the heavy *r*-process elements gadolinium (Gd, $Z = 64$), dysprosium (Dy, $Z = 66$), and thorium (Th, $Z = 90$) in a sample of 276 Galactic disc stars ($-1.0 <$ [Fe/H] $< +0.3$). The stellar spectra have a high resolution of 42 000 and 75 000, and the signal-to-noise ratio higher than 100. The LTE abundances of Gd, Dy, and Th have been determined by comparing the observed and synthetic spectra for three Gd lines (149 stars), four Dy lines (152 stars), and the Th line at 4019.13 Å (170 stars). For about 70 per cent of the stars in our sample, Gd and Dy are measured for the first time, and Th for 95 per cent of the stars. Typical errors vary from 0.07 to 0.16 dex. This paper provides the first extended set of Th observations in the Milky Way disc. Together with europium (Eu, $Z = 63$) data from our previous studies, we have compared these new observations with nucleosynthesis predictions and Galactic Chemical Evolution simulations. We confirm that [Gd/Fe] and [Dy/Fe] show the same behaviour of Eu. We study with GCE simulations the evolution of [Th/Fe] in comparison with [Eu/Fe], showing that unlike Eu, either the Th production is metallicity dependent in case of a unique source of the r-process in the Galaxy, or the frequency of the Th-rich r-process source is decreasing with the increase in [Fe/H].

Key words: stars: abundances – stars: late-type – Galaxy: disc – Galaxy: evolution.

1 INTRODUCTION

The nucleosynthesis of heavy neutron-capture elements in stars and their observations is one of the main research drivers for modern nuclear astrophysics. In this context, the origin of the rapid neutron-capture process (*r*-process, e.g. Cowan et al. 2021, and references therein) is still a major matter of debate. Among others, the most favoured *r*-process sites are neutron-star mergers (e.g. Eichler et al. 1989; Freiburghaus, Rosswog & Thielemann 1999; Goriely et al. 2015; Thielemann et al. 2017; Rosswog et al. 2018) and neutron star-black hole mergers (e.g. Lattimer & Schramm 1974; Surman et al. 2008; Fernández, Foucart & Lippuner 2020), certain rare classes of fast-rotating supernovae with powerful magnetic fields (e.g. Symbalisty, Schramm & Wilson 1985; Cameron 2003; Nishimura et al. 2006; Winteler et al. 2012; Nishimura et al. 2017; Mösta et al. 2018; Obergaulinger, Just & Aloy 2018; Reichert et al. 2021), as well as hypernovae or collapsars (e.g. Cameron 2003; Siegel, Barnes & Metzger 2019; Thielemann, Wehmeyer & Wu 2020; Zenati et al. 2020; Brauer et al. 2021). In the past, core-collapse supernovae (CCSNe) have been considered as the dominant source of the *r* process, initially by suggesting neutron-rich innermost ejecta (e.g. Hillebrandt, Takahashi & Kodama 1976), later arguing for fast (α, n)-reactions in explosive burning of He shells (e.g. Truran, Cowan & Cameron 1978; Thielemann, Arnould & Hillebrandt 1979; Cowan, Cameron & Truran 1985), and afterwards turning to high entropy conditions in neutrino-driven winds during the core-collapse and explosion phase (e.g. Woosley et al. 1994; Takahashi, Witti & Janka 1994; Hoffman, Woosley & Qian 1997; Ning, Qian & Meyer 2007; Farouqi et al. 2010; Arcones & Thielemann 2013). At present, realistic CCSN simulations do not provide the right conditions to

★ E-mail: tmishenina@ukr.net (TM); mpignatari@gmail.com (MP)
† The NuGrid collaboration, http://www.nugridstars.org.

produce a complete *r*-process pattern, while still a mild weak *r*-process production could be possible (see e.g. Wanajo, Janka & Kubono 2011; Curtis et al. 2019; Cowan et al. 2021; Ghosh, Wolfe & Fröhlich 2022).

Stellar spectroscopic observations can be used to derive fundamental constraints for theoretical simulations. In particular, a large number of works in the past decade has been made to define the composition of old *r*-process-rich stars, formed in the early Milky Way Galaxy (e.g. Sneden et al. 2003; Simmerer et al. 2004; Beers & Christlieb 2005; Barklem et al. 2005; Yong et al. 2013; Roederer et al. 2014; Sakari et al. 2018; Mashonkina & Christlieb 2014; Hansen et al. 2018). Such an importance is primarily due to the possibility to trace contributions of one or several stellar sites of production of these elements within the early Galaxy time-scales, before global gas mixing might actually take place (e.g. Hansen et al. 2020). Therefore, stellar observations can be used to test directly *r*-process predictions from different stellar sites (Farouqi et al. 2022) – for instance, those resulting from neutron-star mergers (Ji, Drout & Hansen 2019) or from magnetorotational hypernovae (Yong et al. 2021). This includes to study the role of progenitors of satellite galaxies on the early galactic chemical enrichment (e.g. Gudin et al. 2021).

As the Galaxy evolves, new stars are forming enriched by previous stellar generations. Compared to the early Galaxy, different stellar sources need to be taken into account for the production of neutron-capture elements during the chemical evolution of the Galaxy (GCE; e.g. Prantzos et al. 2018; Kobayashi, Karakas & Lugaro 2020). At present in the Milky Way there are two main processes responsible for the production of heavy elements. In addition to the *r*-process, the slow neutron-capture process (*s*-process, e.g. Käppeler et al. 2011) is responsible for about half of the abundances beyond iron in the Solar system. The *s*-process elements are mainly produced in massive stars (e.g. The, El Eid & Meyer 2007; Pignatari et al. 2010; Frischknecht et al. 2016; Limongi & Chieffi 2018) and asymptotic giant branch (AGB) stars (e.g. Gallino et al. 1998; Busso, Gallino & Wasserburg 1999; Bisterzo et al. 2014; Cristallo et al. 2015; Karakas & Lugaro 2016; Battino et al. 2019). In order to take into account the *r*-process contribution in GCE calculations, these yields are often derived from the solar residual method: the *r*-process abundance pattern is obtained from the solar composition after removing the *s*-process contribution, and then it is assumed to be the same for all metallicities (e.g. Travaglio et al. 2004; Prantzos et al. 2018). Alternatively, a large range of theoretical *r*-process yields may be adopted. GCE models and simulations are crucial tools to better understand the evolution of *r*-process elements in galaxies (e.g. Wehmeyer, Pignatari & Thielemann 2015; Naiman et al. 2018; van de Voort et al. 2020). In particular, the [Eu/Fe] versus [Fe/H] trend in the Galactic disc has been targeted several times to probe the enrichment time-scales and contribution of neutron star mergers and rare classes of CCSNe. Studies have suggested that neutron star mergers alone cannot reproduce the decreasing trend of Eu when assuming a merger delay-time probability distribution (DTD) in the form of t^{-1} (e.g. Côté et al. 2017b, 2019a; Hotokezaka, Beniamini & Piran 2018; Haynes & Kobayashi 2019; Simonetti et al. 2019). Such an issue, however, can be lifted by implying metallicity-dependent DTDs (e.g. Simonetti et al. 2019), imposing shorter delay times for mergers relative to Type Ia supernovae (SNe Ia; e.g. Matteucci et al. 2014; Wehmeyer et al. 2015; Côté et al. 2017b; Cavallo, Cescutti & Matteucci 2021; Wanajo, Hirai & Prantzos 2021), or adopting different treatments for how *r*-process elements are mixed and distributed within the Galaxy (e.g. Schönrich & Weinberg 2019; Banerjee, Wu & Yuan 2020; Beniamini & Hotokezaka 2020). Another solution to recover the [Eu/Fe] trend is to involve additional sources alongside neutron star mergers for Eu, such as rare supernovae originating from massive stars (e.g. Côté et al. 2019a; Siegel et al. 2019; Kobayashi et al. 2020; Cavallo et al. 2021; Greggio, Simonetti & Matteucci 2021; Farouqi et al. 2022).

Europium is the most extensively studied chemical element produced via the *r*-process in the Galactic disc (according to e.g. Bisterzo et al. 2014), the solar *s*-process contribution is about 6 per cent). Europium abundance in the Galactic disc has been investigated by many researchers (e.g. Mashonkina & Gehren 2001; Reddy et al. 2003; Bensby et al. 2005; Mishenina et al. 2013, etc.). On the other hand, there are only a limited amount of stars with available several *r*-process elements measured together from the same analysis. For instance, in Guiglion et al. (2018) gadolinium and dysprosium were examined together with europium and barium within the frameworks of the AMBRE Project based on high-resolution FEROS, HARPS, and UVES spectra from the ESO archive. The contribution by the *s*-process to the Gd and Dy solar abundances is estimated to be 15.4 and 15.0 per cent, respectively (Bisterzo et al. 2014), i.e. indicating a dominant *r*-process contribution. Gd and Dy abundances in thin and thick discs were investigated by Guiglion et al. (2018) and in solar twins by Spina et al. (2018). Th abundances and the ratios Th/Eu were obtained for thin disc stars to estimate the age of the disc (del Peloso, da Silva & Arany-Prado 2005). The Th abundance is also measured for samples of solar twins stars (Unterborn, Johnson & Panero 2015; Botelho et al. 2019). As a continuation of our previous research focused on studying of the Galactic disc enrichment with neutron-capture elements (Mishenina et al. 2013, 2017, 2019a,b), this paper aims to investigate the abundance distribution of the *r*-process elements Gd, Dy and Th. Our study includes new Gd and Dy measurements for nearly 70 per cent of the stars in our sample. For more than 90 per cent of stars, we present new Th values, and the GCE of the Milky Way disc is done for the first time taking into account both actinide (Th) and lanthanide (Eu, Gd, and Dy) observations.

This paper is organized as follows. The observations and the definition of the main stellar parameters are described in Section 2. The abundance determinations and the error analysis are presented in Section 3. The analysis of the behaviour of elemental abundances in the pattern of the theory of nucleosynthesis and the chemical evolution of the Galaxy is reported in Section 4. Conclusions are drawn in Section 5.

2 OBSERVATIONS AND ATMOSPHERIC PARAMETERS

This study was carried out on an initial list of 276 stars and based on the spectra and atmospheric parameters by Mishenina et al. (2013). The 1.93-m telescope at the Observatoire de Haute-Provence (OHP, France) and the echelle-type spectrograph ELODIE (Baranne et al. 1996) were employed to obtain spectra at the resolving power $R = 42\,000$ in the wavelength range from 4400 to 6800 Å and with the signal-to noise (S/N) better than 100 at 5500 Å. We also used additional spectra from the OHP spectroscopic archive (Moultaka et al. 2004) collected with the SOPHIE spectrograph (Perruchot et al. 2008) and covering a similar wavelength range at the spectral resolution $R = 75\,000$. The complex pre-processing of images available on-line and enabling to obtain spectroscopic data in a digital form was carried out immediately during observations (Katz et al. 1998). The subsequent processing of the studied spectra was performed using the DECH30 software package developed by G.A. Galazutdinov (see http://www.gazinur.com/DECH-software.html). DECH software provides all stages of the CCD echelle spectral

image processing, including bias/background subtraction, flat-field correction (separation), extraction of one-dimensional spectrum from two-dimensional images, diffuse light correction, spectrum addition, and exclusion of cosmic ray features. The programme enables to locate a fiducial continuum, to measure equivalent widths (EWs) of lines by several methods, to determine line positions and shifts and much more besides. In this case, we worked with spectra in the FITS format, using such options as normalization of individual spectra to the local continuum, identification of spectral lines, development of the dispersion curve, measurements of the line depths and EWs, elimination of cosmic ray effects, selection of individual parts of the spectrum, etc. The measured line depths were subsequently used to determine the effective temperature ($T_{\rm eff}$) while the EWs of the neutral and ionized iron lines were measured by the Gaussian profile fitting and employed to derive atmospheric parameters (the surface gravity, log g, and micro-turbulent velocity, $V_{\rm t}$).

The stellar atmospheric parameters for the stars under examination in this work were determined by us in previous studies. The procedures employed to derive the effective temperatures $T_{\rm eff}$, surface gravities log g, and microturbulent velocity $V_{\rm t}$ for the target stars had been described in detail in Mishenina & Kovtyukh (2001) and Mishenina et al. (2004, 2008). In particular, the effective temperatures $T_{\rm eff}$ were determined by calibrating the line-depth ratios for the pairs of spectral lines that have different low-level excitation potentials with the application of the technique introduced and developed by Kovtyukh et al. (2003). For most of metal-poor stars in our sample, $T_{\rm eff}$ were assumed by adjusting the far-wings of the H_α line (Mishenina & Kovtyukh 2001). In Mishenina et al. (2004), we showed that the temperature scales adopted in Mishenina & Kovtyukh (2001) and Kovtyukh et al. (2003) are consistent. The surface gravities, log g, were computed from the ionization equilibrium, which means that similar iron abundances should be obtained from the neutral iron (Fe I) and singly ionized iron (Fe II) lines. In our case, the difference between these values does not exceed 0.03 dex. The microturbulent velocity, $V_{\rm t}$, was derived by factoring out correlations between the iron abundances from Fe I lines and the equivalent widths (EW) of those Fe I lines. We adopted the iron abundance determined from the Fe I lines as the metallicity, [Fe/H]. As is known (e.g Thévenin & Idiart 1999; Shchukina & Trujillo Bueno 2001; Mashonkina et al. 2011; Bergemann et al. 2012), the lines of neutral iron are influenced by the deviations from the LTE in the solar and stellar spectra, and hence, these deviations also affect the iron abundances determined from those lines. However, within the temperature and metallicity ranges of our target stars, the NLTE corrections is less than 0.1 dex (e.g Mashonkina et al. 2011). Thus, both in the case of accepted [Fe/H] as the iron abundance from Fe I lines and also in the case of using the ionization equilibrium method for iron to derived log g, this correction does not exceed the errors in determining of these parameters.

The list of parameter values obtained, as well as their comparison with the results of other authors, has been given in (Mishenina et al. 2004, 2008, 2013). The estimated accuracy of our parameter determinations is as follows: $\Delta(T_{\rm eff}) = \pm 100$ K, $\Delta(\log g) = \pm 0.2$ dex, $\Delta(V_{\rm t}) = \pm 0.2$ km s^{-1}, and $\Delta([{\rm Fe/H}]) = \pm 0.1$ dex. In this paper, we have compared our parameters with those obtained recently in the studies by Guiglion et al. (2018) and Spina et al. (2018), wherein gadolinium and dysprosium abundances were determined, and also those in the studies by del Peloso et al. (2005), who reported europium and thorium abundances (five stars in common with our sample) and Unterborn et al. (2015) for one star in common with our sample (see Table 1). To compare with our findings, we chose the data reported by (Guiglion et al. 2018) for the stars in common with the highest S/N among those available in on-line catalogs. We obtained average differences and errors for 36 stars in common by deducting our data from those by Guiglion et al. (2018) (see Table 1). Then, we sorted out the data with $T_{\rm eff}$ from 5100 to 6300 K and surface gravities within $3.5 < \log g < 5.0$ (for 26 stars in common) as such ranges of parameter values had been chosen by the authors as criteria for the selection of stars for further analysis; the resulting differences are slightly smaller (Table 1). In general, we see a good agreement between our findings and those from the literature, as well as a good consistency with the estimated accuracy in parameter determinations adopted earlier. As we can see from Table 1, the mean difference $\Delta T_{\rm eff}$ between our effective temperature and that obtained by other authors, does not exceed 25 K, and the rms deviations are within 100 K. A mean difference in gravity values $\Delta \log g$ does not exceed 0.10, with the rms deviation is only slightly exceeding (0.22), adopted earlier (0.2). In terms of metallicity, the mean value does not exceed $\Delta([{\rm Fe/H}]) = 0.05 \pm 0.07$ dex.

We adopt the kinematic classification of the stars into the thin and thick discs and Hercules stream, as previously described in (Mishenina et al. 2013). To determine the components of spatial velocity (U, V, W) and the belonging of stars to different galactic populations, the Hipparhos catalogue was used. Since the stars in our sample are bright and tend to have *Gaia* astrometric errors equivalent to those of the *Hipparcos* observations, we have not updated our classification with respect to the latest astrometric data from the Gaia Data Release 2 (Gaia Collaboration 2018). Some stars are even too bright to be measured by *Gaia*. Our previous sample of 276 stars in total consists of 21 stars belonging to the thick disc, 212 of those in the thin disc, 16 stars related to the Hercules stream, and 27 unclassified stars.

3 ABUNDANCE DETERMINATION

The abundances of Dy, Gd, and Th were derived in the local thermodynamical equilibrium (LTE) approximation with a new modified STARSP LTE spectral synthesis code (Tsymbal 1996) using the models by Castelli & Kurucz (2004). For each star, the model was chosen by standard interpolation for $T_{\rm eff}$ and log g. The metalicity [Fe/H] and the turbulent velocity $V_{\rm t}$ are not interpolated, in terms of metallicity, a model close to [Fe/H] of stars in ± 0.2 dex was selected and the turbulent velocity $V_{\rm t}$ determined for each star was used. For Gd II lines 4037.89, 4085.56, 4483.33Å, and Dy II lines 4073.12, 4077.97, 4103.31, and 4449.70 Å, and Th II 4019.12 Å. The oscillator strengths log gf were adopted from last version (2016) of the VALD database (Kupka F. et al. 1999). In contrast to the considered Gd and Dy lines, the 4019.129 Å Th line is a complex blend with a contribution to its intensity from the Th and Co abundances at almost the same wavelength (e.g. del Peloso et al. 2005; Mashonkina, Christlieb & Eriksson 2014; Botelho et al. 2019). Using a list of VALD lines, which includes atomic and molecular lines, to describe the Th line in the solar spectrum, we found a noticeable discrepancy between the observed and calculated spectra in the region of Fe lines; to eliminate this, we corrected the log gf Fe I oscillator strengths with an appropriate fit. The values of the oscillator strength adopted by us for the Th and Co lines follow the VALD list, namely the values of log $gf = -0.228$ for the Th II line (Nilsson et al. 2002) and -2.270 for the Co I line (Lawler, Whaling & Grevesse 1990), in our case, they are presented with a detailed contributions of the hyperfine structure. A list of our main atomic and molecular lines employed in the thorium 4019 Å line region are given in Table 2. For the Sun, and two stars with stellar parameters ($T_{\rm eff}$, log g, [Fe/H]) HD 22879 (5825; 4.42; -0.91), and HD (5373; 4.30; 0.25) the predominant

Table 1. Comparison of parameters and Eu, Gd, Dy, and Th abundance determinations taken from the literature with our results for the *n* stars common with our stellar sample.

Reference	$\Delta(T_{\rm eff})$	$\Delta(\log g)$	Δ([Fe/H])	Δ([Eu/Fe])	Δ([Gd/Fe])	Δ([Dy/Fe])	Δ([Th/Fe])	*n*
Guiglion et al. (2018)	-14.7 ± 99.4	0.09 ± 0.22	0.01 ± 0.07	0.09 ± 0.16	0.09 ± 0.18	0.14 ± 0.16	–	36
Guiglion et al. (2018)	12.1 ± 93	0.06 ± 0.21	0.0 ± 0.07	0.09 ± 0.15	0.03 ± 0.13	0.10 ± 0.13	–	26
Spina et al. (2018)	14.8 ± 25	0.06 ± 0.1	0.04 ± 0.05	-0.03 ± 0.04	-0.03 ± 0.04	-0.04 ± 0.05	–	6 (4)
del Peloso et al. (2005)	-16.4 ± 55	0.04 ± 0.08	0.05 ± 0.08	0.05 ± 0.08	–	–	-0.23 ± 0.14	5 (4)
Morell et al. (1992)	-3.8 ± 85	0.02 ± 0.20	-0.02 ± 0.04	–	–	–	-0.11 ± 0.12	5 (5)
Unterborn et al. (2015)	23	0.05	0.04	–	–	–	0.48	1(1)
Botelho et al. (2019)	-15.6 ± 28	-0.05 ± 0.11	-0.04 ± 0.05	0.02 ± 0.04	–	–	-0.09 ± 0.15	5(3)

Note. Our data for Eu abundances are from Mishenina et al. (2013).

Table 2. List of lines in the thorium 4019 Å line region.

Species	Lambda, Å	Elow, ev	log *gf*	Source
Ce II	4018.820	1.55	−0.959	VALD
Nd II	4018.820	0.06	−0.890	VALD
Fe I	4018.887	4.26	−2.781	Solar fit
Ce II	4018.900	1.01	−1.219	VALD
Ce II	4018.927	0.63	−1.679	VALD
V I	4018.929	2.58	−0.556	VALD
Pr II	4018.963	0.20	−1.029	VALD
13CH	4018.965	0.46	−3.253	VALD
Mn I	4018.987	4.35	−1.883	VALD
Fe I	4019.002	4.32	−2.700	solar fit
Fe I	4019.042	2.61	−3.100	solar fit
V II	4019.044	3.75	−1.231	VALD
Ce II	4019.057	1.01	−0.529	VALD
Mn I	4019.066	4.67	−0.522	VALD
Ni I	4019.067	1.94	−3.399	VALD
13CH	4019.074	0.46	−3.245	VALD
Co I	4019.110	2.28	−3.287	VALD
Co I	4019.118	2.28	−3.173	VALD
Co I	4019.120	2.28	−2.876	VALD
Co I	4019.125	2.28	−3.492	VALD
Co I	4019.126	2.28	−3.298	VALD
Th II	4019.129	0.00	−0.227	VALD
Co I	4019.129	2.87	−5.163	VALD
V I	4019.134	1.80	−2.149	VALD
Co I	4019.135	2.28	−3.287	VALD
Co I	4019.135	2.28	−3.474	VALD
Co I	4019.138	2.28	−3.173	VALD
Co I	4019.140	2.28	−3.298	VALD
Co I	4019.143	2.87	−5.142	VALD
Co I	4019.210	2.87	−4.821	VALD

lines in the region are shown in Fig. 1. Examples of fitting several Gd, Dy, and Th lines in the stellar spectra are presented in Fig. 2.

In order to calculate the synthetic spectrum and the Th abundance, we used the relevant abundances of chemical elements obtained by Mishenina et al. (2013), including nickel. In particular, to take into account the blend due to cobalt, as a first approximation, we estimated its abundance from the scaled solar cobalt value. Then, we further refined from the profile fit of the cobalt line at a wavelength of 4020.89 Å, which was calculated factoring in the hyperfine structure (HFS). We finally derived the Th abundance by taking into account the contribution of cobalt in the blend Th-Co. Therefore, our results obtained for thorium should not be overestimated because of local contribution from other elements. Examples of fitting Co line in the stellar spectra are shown in Fig. 8. The abundance of europium was determined by us early and for further analysis in this study, we use those obtained in Mishenina et al. (2013). In that study, the Eu

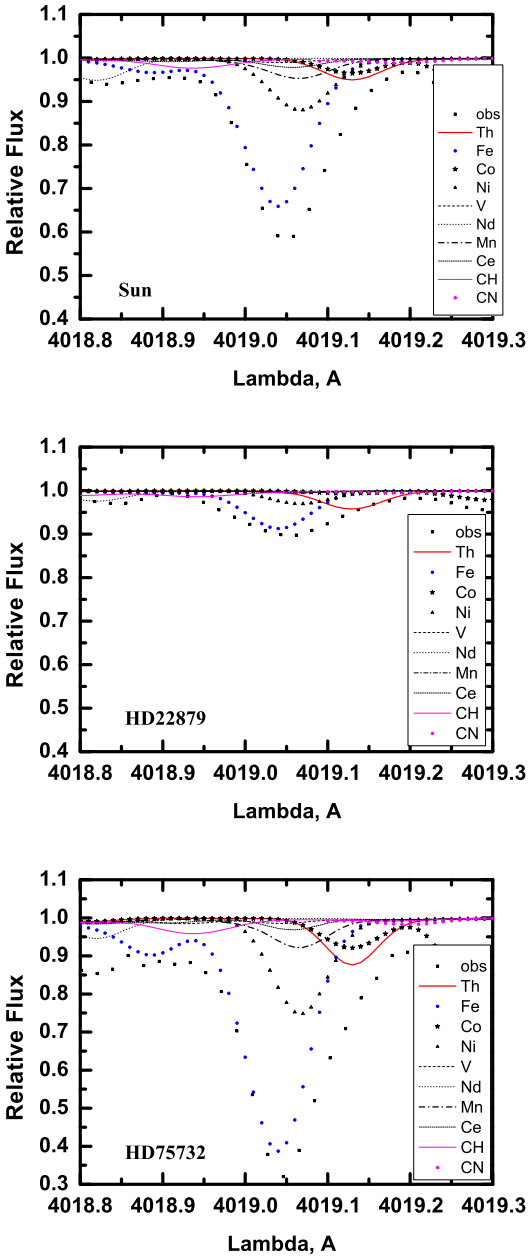

Figure 1. Observed (squares) and calculated spectra in the region of Th II line for Sun, HD 22879 (5825; 4.42; −0.91), and HD 75732 (5373; 4.30; 0.25). The contributions of various elements to the profile of the thorium line are marked on the panel.

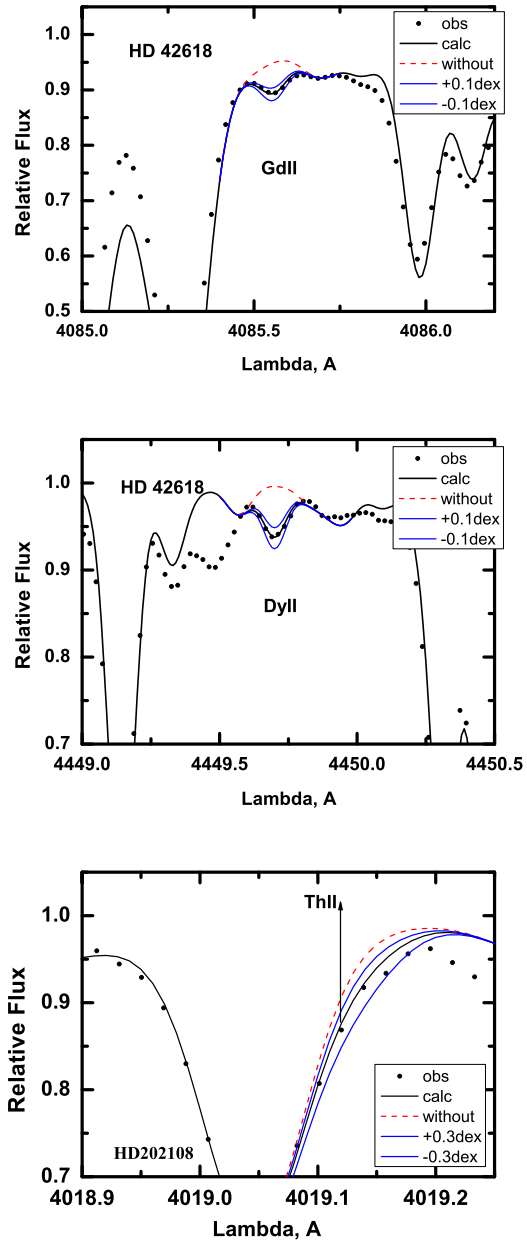

Figure 2. Observed (points) and calculated spectra in the region of Gd II, Dy II, and Th II lines for stars HD 42018 (5787; 4.5; –0.07) and HD 202108 (5712; 4.2; –0.21).

abundance was derived from the Eu II lines at 6645 Å, taking into account the HFS (Ivans et al. 2006). The solar abundances of Dy, Gd, and Th are determined using the STARSP code (Tsymbal 1996) from the lines in the spectra of the Moon and asteroids obtained with the ELODIE spectrograph with the line parameters being the same as in the stellar spectra: log A(Gd) = 1.08 ± 0.05 and log A(Dy) = 1.10 ± 0.05, which coincide with Asplund et al. (2009) (log $A(Gd)_{\odot}$ = 1.07 ± 0.04, log $A(Dy)_{\odot}$ = 1.10 ± 0.04), and our solar log A(Th) = 0.08 ± 0.08 is consistent with the value log $A(Th)_{\odot}$ = 0.08 reported for the Sun in (Mashonkina et al. 2014), the value of Asplund et al. (2009) is log $A(Th)_{\odot}$ = 0.02 ± 0.10.

The stellar parameters and obtained Gd, Dy, and Th abundances with the statistical uncertainties associated from line-to-line abundance variation (standard deviation or rms derivation) are given in Table A1.

Table 3. Abundance errors due to atmospheric parameter uncertainties, for four stars with different set of stellar parameters ($T_{\rm eff}$, log g, $V_{\rm t}$, [Fe/H]): HD154345 (5503, 4.30, 1.3, −0.21), HD82106 (4827, 4.10, 1.1, −0.11), HD75732 (5373, 4.30, 1.1, 0.25), and HD201891 (5850, 4.40, 1.0, −0.96).

AN	El	Δ $T_{\rm eff}$ +	Δ log g +	Δ $V_{\rm t}$ +	tot +
		HD1545345			
64	Gd II	0.07	0.10	0.01	0.12
68	Dy II	0.09	0.08	0.02	0.13
90	Th II	0.10	0.11	0.0	0.16
		HD82106			
64	Gd II	0.07	0.06	0.00	0.10
68	Dy II	0.10	0.12	0.01	0.15
90	Th II	0.05	0.06	0.0	0.11
		HD75732			
64	Gd II	0.06	0.10	0.01	0.12
68	Dy II	0.10	0.09	0.01	0.14
90	Th II	0.10	0.06	0.0	0.14
		HD201891			
64	Gd II	0.02	0.04	0.02	0.08
68	Dy II	0.05	0.03	0.01	0.07
90	Th II	0.12	0.06	0.0	0.15

3.1 Errors in abundance determinations

The total errors in Gd, Dy, Th abundance determinations mainly result from the errors in sampling the parameter values and fitting the synthetic spectra to observational ones (0.05 dex in Gd and Dy, and 0.08 for Th). To determine the systematic errors in the elemental abundances, resulting from uncertainties in the atmospheric parameters, we derived the elemental abundance of four stars with different set of stellar parameters ($T_{\rm eff}$ in K, log g, $V_{\rm t}$ in km s^{-1}, [Fe/H]): HD154345 (5503, 4.30, 1.3, −0.21), HD82106 (4827, 4.10, 1.1, −0.11), HD75732 (5373, 4.30, 1.1, 0.25), and HD201891 (5850, 4.40, 1.0, −0.96) for several models with modified parameters ($\Delta T_{\rm eff}$ = + 100 K, Δlog g= +0.2, $\Delta V_{\rm t}$ = + 0.1). The impact of the parameter uncertainties on the accuracy of elemental abundance determinations, as exemplified by the stars with different $T_{\rm eff}$ and metallicities, is presented in Table 3.

As can be seen from Table 3, uncertainties in $T_{\rm eff}$ and log g contribute maximally to the total error. Total errors due to parameter uncertainties and the measured spectra vary from 0.07 to 0.15 dex for Gd and Dy, and from 0.11 to 0.16 dex for Th abundance.

To verify our selection of stellar parameters, we present correlations between Gd, Dy and Th abundances and atmospheric parameters $T_{\rm eff}$ and log g (see Figs 3 and 4). As can be seen in Figs 3 and 4, there is no correlation between the elemental abundances and chosen parameters.

A comparison between the abundance determinations obtained in this study and the data reported by other authors is given in Table 1 (see in Section 2). Also Fig. 5 shows our [Eu/Fe], [Gd/Fe], and [Dy/Fe] data and ones from Guiglion et al. (2018) and Spina et al. (2018) as a function of [Fe/H]. For these Figures we selected the data of Guiglion et al. (2018) with $T_{\rm eff}$ from 5100 to 6300 K and surface gravities within 3.5 < log g< 5.0. Such ranges of parameter values are the same chosen by the authors for further analysis. Fig. 6 presents our [Th/Fe] determinations and those by del Peloso et al. (2005), Morell, Kallander & Butcher (1992), Unterborn et al. (2015), and Botelho et al. (2019). Fig. 7 also shows the stellar velocity along

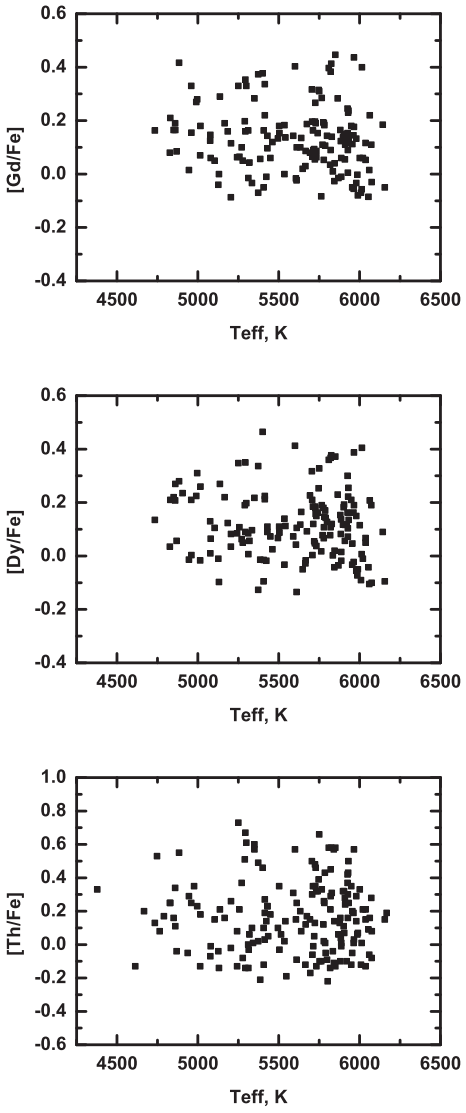

Figure 3. Dependence of [El/Fe] versus $T_{\rm eff}$.

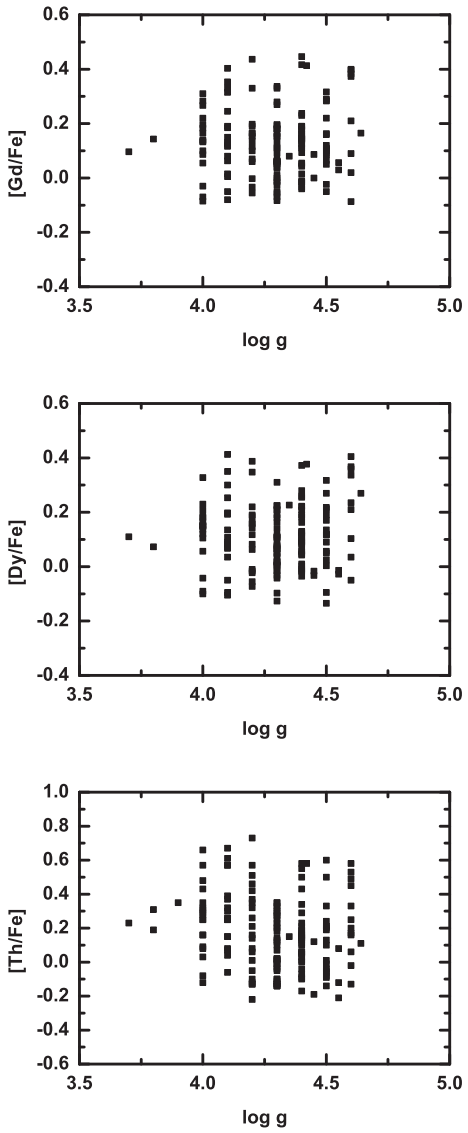

Figure 4. Dependence of [El/Fe] versus log g.

the Z axis with respect to [Th/Fe] and [Th/Eu] for thin and thick disk stars in our observed sample. There is no evidence about different abundance trends between these two groups of stars, also taking into account the more limited statistics available for our thick disk stars.

Table 1 shows the mean differences and rms errors for the values of thorium abundance obtained by us and other authors for stars in common. We have five common stars with Morell et al. (1992), for which the parameters and content of thorium are determined: Δ([Th/Fe]) (our − Morell) = 0.11 ± 0.12 dex, the shift is within the error limits. We also have five stars in common with del Peloso et al. (2005), for which parameters have been determined, and four of them have definitions of thorium abundance. The mean difference is Δ([Th/Fe]) (our − Peloso) = 0.23 ± 0.14 dex and it is larger than the resulting error. In addition, there is one star HD 76932 also shared with Morell et al. (1992) and del Peloso et al. (2005). Our thorium abundance for HD 76932 is [Th/Fe] = 0.57 dex, and Morell et al. (1992) and del Peloso et al. (2005) give [Th/Fe] = 0.35 and 0.30 dex, respectively. There is one common star, namely HD 146233, with Unterborn et al. (2015), which is also was studied by Botelho et al. (2019). For HD 146233, the Th measurements are varying significantly between different works. We obtain [Th/Fe] = –0.09 dex, Unterborn et al. (2015) give [Th/Fe] = 0.28 dex, and in Botelho et al. (2019), [Th/Fe] = 0.15 dex. We have five stars in common with the Botelho et al. (2019), but among them only three stars have measurements of Th abundance. The mean difference and rms between our data and those of Botelho et al. (2019) is Δ([Th/Fe]) (our − Botelho) = −0.09 ± 0.15. This value (shift) has opposite sign in comparison with those obtained for comparison of Morell et al. (1992), and del Peloso et al. (2005), but it is within the limits of errors. From a comparison with Morell et al. (1992), del Peloso et al. (2005), and Botelho et al. (2019), the obtained rms of the mean difference are 0.12, 0.14, and 0.15, respectively. At the same time, the del Peloso et al. (2005) data show a systematic shift relative to our data (0.23), since the mean difference is greater than the scatter. The maximum difference in thorium abundance between our values and these for del Peloso et al. (2005) reaches 0.4 dex for the star HD 22879. However, this discrepancy is contributed also by a difference of 0.15 dex in metallicity obtained by us ([Fe/H] = −0.91 and −0.76; del Peloso et al. 2005). Fig. 8 (top panel)

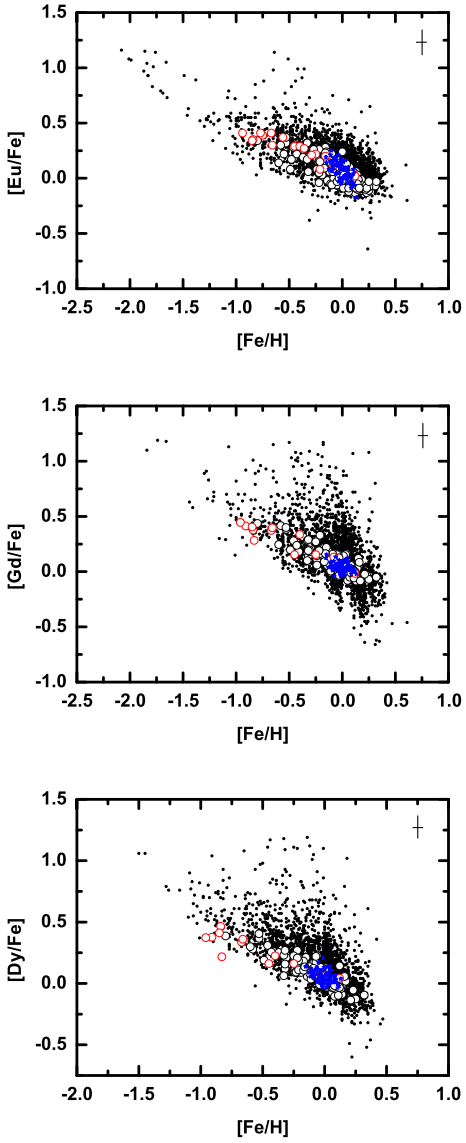

Figure 5. [Eu/Fe], [Gd/Fe], and [Dy/Fe] as a function of [Fe/H]. Stars associated with the thin and thick discs are marked as black and red open circles, respectively. Selected data are taken from Guiglion et al. (2018) (points), and ones from Spina et al. (2018) (asterisks).

presents the synthetic spectra for the star HD 22879 calculated in this work (blue solid line) and that with the data (stellar parameters, chemical abundances and line list) of (del Peloso et al. 2005) (red solid line). The black solid line shows the calculation from our data (parameters, abundance), but adapted to the Peloso's line list. Blue asterisks shows the calculation based on Peloso's data (parameters, abundances) with our line list in the thorium region. Circles are the corresponding observational spectrum. The bottom panel shows a description of the observed spectrum by our synthetic spectrum in a wider spectral region with the thorium line. We observe a difference in the synthetic calculations for our data and those of (del Peloso et al. 2005) in the region of the iron, nickel, manganese lines at the maximum intensity of this spectral peculiarity due to the difference in oscillator strengths of lines, assumed abundances of elements and the absence of the iron line in the (del Peloso et al. 2005) list. In the part of profile with the thorium-cobalt lines, we see that using our

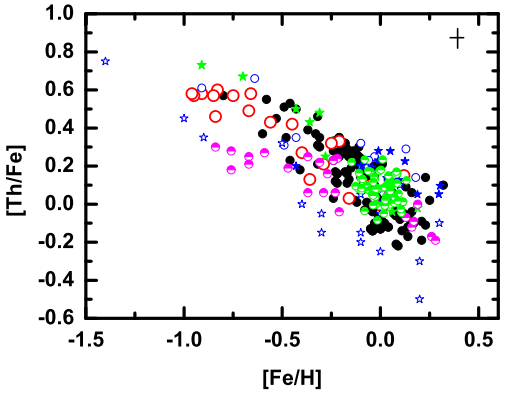

Figure 6. [Th/Fe] as a function of [Fe/H]. Our measurements associated with the thin and thick discs are marked as black circles and red open circles, respectively. In comparison, observations by del Peloso et al. (2005) (blue open circles), Morell et al. (1992) (blue open asterisks), Unterborn et al. (2015) (blue asterisks), and Botelho et al. (2019) (green semi-full circles) are shown.

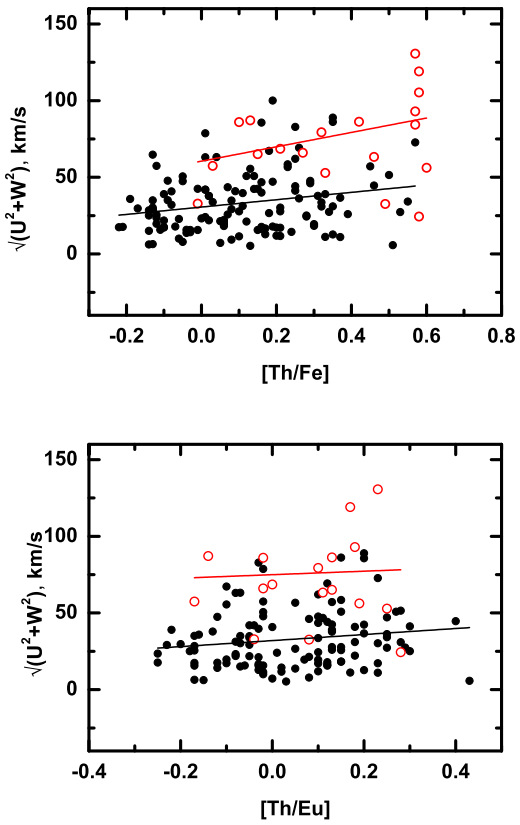

Figure 7. For our stellar sample, the velocities along the Z-axis ($\sqrt{U^2+W^2}$) are shown with respect to [Th/Fe] and [Th/Eu]. The full sample is divided between thick and thin disc stars.

data and different line lists gives similar trends, and different stellar parameters and abundances make a significant contribution to the result, in this case, an increase in the thorium abundance compared to that obtained by (del Peloso et al. 2005) is required. In general, the differences between the data obtained in different works are mostly due to the different lists of used lines in the thorium line region and different parameters and elemental abundances measured in different works.

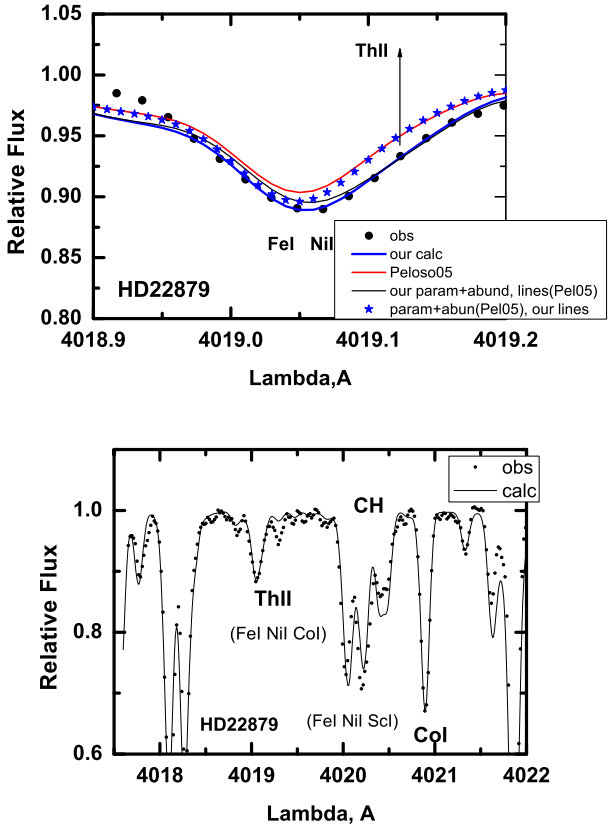

Figure 8. Top panel: comparison of the synthetic spectrum calculations for our data and those of Peloso et al. (2005) (see details in the text); bottom panel: comparison of our synthetic computation with observations, in the region of Th II line for a wider range of the spectrum.

4 RESULTS AND COMPARISON WITH GALACTIC CHEMICAL EVOLUTION MODELS

The Milky Way disc stars with the metallicity range covered from this study are formed from interstellar matter enriched by several generations of stars. Therefore, these observations cannot be directly compared with theoretical stellar models, and Galactic chemical evolution (GCE) simulations must be used to study the evolution history that allowed to build the chemical inventory observed today (e.g. Tinsley 1980; Gibson et al. 2003; Kobayashi et al. 2020; Matteucci 2021, and references therein). In this work we focus on the *r*-process elements Eu, Gd, Dy, and Th. Although the main stellar source of the *r* process in the Galaxy is still matter of debate, since decades, the *r* process was typically considered to produce the same abundances independently from the metallicity of the stellar progenitors. The close similarity between the solar residual (where the residual is derived by subtracting the *s*-process contribution from the solar abundances of heavy elements beyond iron; e.g. Arlandini et al. 1999; Bisterzo et al. 2014; Prantzos et al. 2020) and the abundance patterns measured in *r*-process-rich metal-poor stars drove and supported such a scenario. Indeed, while there is a significant abundance scatter among different *r*-process-enriched stars for lighter elements in the mass region Sr-Ru, the abundances appear to better align with the solar residual for Ba and heavier elements up to Pb (e.g. Sneden, Cowan & Gallino 2008; Cowan et al. 2021). Within this heavier mass region, GCE simulations could carry the same *r*-process signature across the evolution of the Galaxy, where the main remaining uncertainties are the source frequency and the quantitative *r*-process yields associated to each stellar source (e.g. Matteucci et al. 2014; Wehmeyer et al. 2015; Hotokezaka et al. 2018; Côté et al. 2018a). A larger observational scatter between different *r*-process-rich stars has been measured for the actinides elements Th and U, which are highly affected by varying the conditions in *r*-process theoretical calculations (Eichler et al. 2019; Cowan et al. 2021). However, a significant variation is also seen beyond Ba once a larger sample of metal-poor stars is considered (Roederer et al. 2010), suggesting that the *r*-process production does not yield a unique and robust pattern, and a degree of variation should be expected. The observation of actinide-boost stars has further questioned those classical paradigms (e.g. Roederer et al. 2010; Holmbeck et al. 2018; Farouqi et al. 2022).

At least for metal-poor halo stars in the Galaxy, it is still matter of debate if only one *r*-process source would be able to explain the early large variations observed in stars for Eu and other heavy *r*-process element abundances with respect to iron or α-elements. As already pointed out by Qian & Wasserburg (2007) and followed up by Hansen, Montes & Arcones (2014), it is actually more plausible that at least two different types of r-process sources were active, contributing with different frequencies and time-scales. Here we discuss the aspect that two processes contribute to the lanthanide and actinide *r*-process elements. On the other hand, observations from old metal-poor stars would not exclude that today there is one source with possible abundance variations, dominating the *r*-process contribution to GCE (e.g. Wehmeyer et al. 2015; Côté et al. 2019a; Farouqi et al. 2022, and references therein).

If we consider the *r*-process lanthanides discussed in this work, i.e. Eu, Gd, and Dy, we have seen in Fig. 5 that their abundance trends with respect to Fe are similar. In particular, we cannot identify if the observed abundance scatter is due to the GCE contribution from multiple *r*-process sources and/or some different production in the region, or if such a dispersion can be simply due to observation uncertainties.

On the other hand, it may be interesting to study the evolution of Th (an actinides element) with respect to Eu. In this context, we have performed GCE models to compare with our new observations. The simulations are made using the PYTHON code OMEGA + (Côté et al. 2017a, 2018b), which is part of the open-source JINAPYCEE package.[1] It consists of a two-zone model that includes a one-zone GCE model surrounded by a large gas reservoir representing the circumgalactic medium. These two zones are interacting via galactic inflows and outflows, where inflows transfer gas from the circumgalactic medium to the central GCE model (the galaxy), and outflows transfer gas from the galaxy to the circumgalactic medium. In this work, we use the yields of Nomoto, Kobayashi & Tominaga (2013), Cristallo et al. (2015), and Iwamoto et al. (1999) for massive stars, low-and intermediate-mass stars, and SNe Ia, and the same galaxy evolution parameters as the best model found in Côté et al. (2019b), which reproduced various observational constraints such as the current star formation rate, gas inflow rate, supernova rates, total stellar mass, and total gas mass. Recent developments have allowed to take into account radioactivity throughout the GCE calculations (Côté et al. 2019b; Trueman et al. 2022), using the numerical solver presented in Yagüe López et al. (2022) to properly follow radioactive decay on time-scales shorter than the lifetime of the Milky Way. This numerical solver was modified in OMEGA + to include the terms for material moving between the two simulated zones along with decay in an unsplit fashion.

[1] https://github.com/becot85/JINAPyCEE.

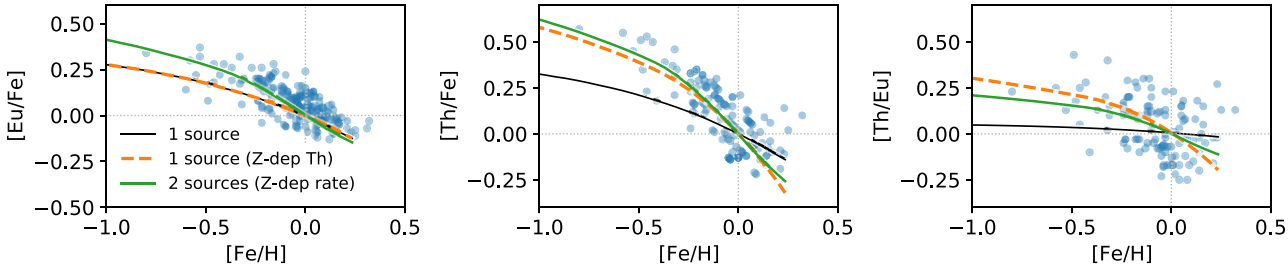

Figure 9. Predicted evolution of [Eu/Fe], [Th/Fe], and [Th/Eu] as a function of [Fe/H] in the Galactic disc, using OMEGA + . In each panel, the solid black line assumes one *r*-process site with a prompt delay, assuming constant Eu and Th yields for all enrichment events. The dashed orange line is the same as the black line, but assuming *Z*-dependent Th yields. The solid green line assumes two *r*-process sites, one with a prompt delay and one with a long-lasting delay-time distribution, where the contribution of the prompt site declines with increasing metallicity.

Our results are shown in Fig. 9, and our goal is to address the relative time-scales at which Eu (as a representative of the *r*-process production of lanthanides including Dy and Gd) and Th (as a representative of the actinides) are produced within the Galactic disc with a simple approach. Given this goal, all Eu and Th yields in our models have been included artificially in order to freely explore which scenarios could give rise to the GCE trends provided by our data. The black solid lines assume that all Eu and Th come from one source, with a short delay time typical of CCSNe sources. Here Eu and Th yields are the same in all events, regardless of metallicity. In this case, while our prediction is acceptable for [Eu/Fe], the predicted trend for [Th/Fe] does not decrease as steeply as the observational data, a feature that can also be seen with [Th/Eu]. The relatively flat [Th/Eu] trend shows that the decay of Th (the ^{232}Th half-life is 14.1 billion years) plays an insignificant role in shaping our predictions, meaning that Th decay would not explain the different degrees at which Th and Eu decrease with respect to metallicity.

The dashed orange and solid green lines in Fig. 9 explore two different scenarios matching the Th and Eu trends simultaneously. The dashed orange line still assumes one prompt *r*-process source and a constant yield for Eu, but assumes metallicity-dependent Th yields where Th is boosted by a factor of 4.5 at low metallicity relative to high metallicity, with a continuous decrease between $Z = 0.001$ and 0.02. The solid green line, on the other hand, combines two *r*-process sources – neutron star mergers with long delay times, and exotic SNe or collapsars with short delays (see also e.g. Côté et al. 2019a; Haynes & Kobayashi 2019; Siegel et al. 2019; Farouqi et al. 2022; Molero et al. 2021). In this case, Th and Eu yields are kept constant as a function of metallicity for both sources. However, the frequency of the short-delay source is assumed to be metallicity dependent, such that its rate is three times higher than the long-delay source at $Z < 0.001$, and becomes negligible $Z > 0.01$. Such a computational experiment would boost the Th production at low metallicity as we may expect. A type of exotic SNe that would fit these assumptions are magneto-rotational (MHD) supernovae. MHD supernovae were originally proposed as a source of a strong *r*-process (e.g. Winteler et al. 2012). However, it was later shown by Mösta et al. (2018) that a strong *r*- process can only be obtained with (unlikely) very extreme pre-collapse magnetic fields, which are required to eject neutron-rich matter stemming from the electron capture during the collapse to high densities. If sufficient rotation exists also weaker pre-collapse magnetic fields can be enhanced by the magneto-rotational instability (MRI), lead to a successful explosion and a highly magnetized neutron star (magnetar), but during the delay encountered before the MRI had its impact, neutrino absorptions enhance the electron fraction and limit the reach of the *r*-process. On the other hand, black hole accretion disc outflows can lead to highly *r*-process-enriched matter with Y_e-values in the ejecta just in the range leading to an actinide boost, as observed in many r-II stars (see the detailed discussion in Farouqi et al. 2022). As the collapsar behaviour leading to black holes requires the core-collapse of quite massive progenitors, their frequency is expected to be much higher at low metallicities. The reason is that low-metallicity progenitors have lower opacities, experience – as a consequence – less mass-loss during their stellar evolution and possess at the point of core collapse significantly higher masses, favoring the collapse to a black hole.

Both scenarios shown in Fig. 9 lead to an enhancement of Th production in the early Universe, and would both be consistent with the observation of metal-poor actinide-boost stars. From this time-scale experiment, it is unfortunately not possible to distinguish between one *r*-process source with metallicity-dependent yields, multiple *r*-process sources with metallicity-dependent rates, or a combination of the two. The variations observed in metal-poor stars between *r*-process elements and the existence of the actinide-boost stars seem to point more toward the second or third scenarios mentioned above (e.g. Roederer et al. 2010; Farouqi et al. 2022) that, as we have seen, it would be consistent with observations at higher metallicities in the Galactic disc. Nevertheless, the fact that [Th/Fe] decreases more steeply than [Eu/Fe] suggests that Th and Eu had a different production history, with Th being more efficiently synthesized at low metallicity than at high metallicity, as compared to Eu.

5 CONCLUSIONS

In this work, we presented and discussed the abundance measurements of Gd, Dy and Th for 276 disc stars. The analysis is based on LTE assumptions. Typical uncertainties are 0.10 dex for Gd (with a range between 0.08 and 0.12 dex), 0.11 dex for Dy (between 0.07 and 0.15 dex), and 0.12 dex for Th (with a range between 0.09 and 0.15 dex). The major sources of these uncertainties in the analysis are the stellar surface temperature and gravities.

The [Dy/Fe] and [Gd/Fe] ratios show the same trend of [Eu/Fe] in the galactic disc. Due to the present observation uncertainties, it is not possible to use the evolution of Dy and Gd with respect to Eu to disentangle a contribution from different *r*-process components. On the other hand, [Th/Fe] shows a steeper decrease than the [Eu/Fe] with respect to [Fe/H].

By using GCE models, we have explored possible solutions to explain those trends. We found that the observations may be better reproduced by one *r*-process source but with metallicity-dependent Th yields, or by multiple *r*-process sources with metallicity-dependent rates for the Th-rich source. We would rather support this second

scenario, since it would also be compatible with observations of both actinides boost *r*-process-rich metal-poor stars and not boosted.

ACKNOWLEDGEMENTS

This paper was based on observations collected at OHP Observatory, France. MP acknowledges significant support to NuGrid from NSF grant PHY-1430152 (JINA Center for the Evolution of the Elements) and STFC (through the University of Hull's Consolidated Grant ST/R000840/1), and access to VIPER, the University of Hull High Performance Computing Facility. MP acknowledges the support from the 'Lendület-2014' Programme of the Hungarian Academy of Sciences (Hungary). FKT acknowledges support from the European Research Council (FP7) under ERC Advanced Grant Agreement 321263 FISH. BC, AY, and MP acknowledge support from the ERC Consolidator Grant (Hungary) funding scheme (project RADIOSTAR, G.A. n. 724560) and from the National Science Foundation (USA) under grant No. PHY-1430152 (JINA Center for the Evolution of the Elements). This paper is based upon work from the ChETEC COST Action (CA16117), supported by COST (European Cooperation in Science and Technology). We thank the ChETEC-INFRA project funded from the European Union's Horizon 2020 research and innovation programme (grant agreement No. 101008324), and the IReNA network supported by NSF AccelNet. MP also thank the UK network BRIDGCE. TM is grateful to the Laboratoire d'Astrophysique de l'Universite de Bordeaux for their kind hospitality.

DATA AVAILABILITY

The data underlying this paper will be shared on reasonable request to the corresponding author.

REFERENCES

Arcones A., Thielemann F.-K., 2013, J. Phys. G: Nucl. Phys., 40, 013201
Arlandini C., Käppeler F., Wisshak K., Gallino R., Lugaro M., Busso M., Straniero O., 1999, ApJ, 525, 886
Asplund M., Grevesse N., Sauval A. J., Scott P., 2009, ARA&A, 47, 481
Banerjee P., Wu M.-R., Yuan Z., 2020, ApJ, 902, L34
Baranne A. et al., 1996, A&AS, 119, 373
Barklem P. S. et al., 2005, A&A, 439, 129
Battino U. et al., 2019, MNRAS, 489, 1082
Beers T. C., Christlieb N., 2005, ARA&A, 43, 531
Beniamini P., Hotokezaka K., 2020, MNRAS, 496, 1891
Bensby T., Feltzing S., Lundström I., Ilyin I., 2005, A&A, 433, 185
Bergemann M., Lind K., Collet R., Magic Z., Asplund M., 2012, MNRAS, 427, 27
Bisterzo S., Travaglio C., Gallino R., Wiescher M., Käppeler F., 2014, ApJ, 787, 10
Botelho R. B. et al., 2019, MNRAS, 482, 1690
Brauer K., Ji A. P., Drout M. R., Frebel A., 2021, ApJ, 915, 81
Busso M., Gallino R., Wasserburg G. J., 1999, ARA&A, 37, 239
Cameron A. G. W., 2003, ApJ, 587, 327
Castelli F., Kurucz R. L., 2004, A&A, 419, 725
Cavallo L., Cescutti G., Matteucci F., 2021, MNRAS, 503, 1
Côté B., O'Shea B. W., Ritter C., Herwig F., Venn K. A., 2017a, ApJ, 835, 128
Côté B., Belczynski K., Fryer C. L., Ritter C., Paul A., Wehmeyer B., O'Shea B. W., 2017b, ApJ, 836, 230
Côté B. et al., 2018a, ApJ, 855, 99
Côté B., Silvia D. W., O'Shea B. W., Smith B., Wise J. H., 2018b, ApJ, 859, 67
Côté B. et al., 2019a, ApJ, 875, 106
Côté B., Lugaro M., Reifarth R., Pignatari M., Világos B., Yagüe A., Gibson B. K., 2019b, ApJ, 878, 156
Cowan J. J., Cameron A. G. W., Truran J. W., 1985, ApJ, 294, 656
Cowan J. J., Sneden C., Lawler J. E., Aprahamian A., Wiescher M., Langanke K., Martínez-Pinedo G., Thielemann F.-K., 2021, Rev. Mod. Phys., 93, 015002
Cristallo S., Straniero O., Piersanti L., Gobrecht D., 2015, ApJS, 219, 40
Curtis S., Ebinger K., Fröhlich C., Hempel M., Perego A., Liebendörfer M., Thielemann F.-K., 2019, ApJ, 870, 2
del Peloso E. F., da Silva L., Arany-Prado L. I., 2005, A&A, 434, 301
Eichler D., Livio M., Piran T., Schramm D. N., 1989, Nature, 340, 126
Eichler M., Sayar W., Arcones A., Rauscher T., 2019, ApJ, 879, 47
Farouqi K., Kratz K.-L., Pfeiffer B., Rauscher T., Thielemann F.-K., Truran J. W., 2010, ApJ, 712, 1359
Farouqi K., Thielemann F.-K., Rosswog S., Kratz K.-L., 2022, A&A, 663, A70
Fernández R., Foucart F., Lippuner J., 2020, MNRAS, 497, 3221
Freiburghaus C., Rosswog S., Thielemann F.-K., 1999, ApJ, 525, L121
Frischknecht U. et al., 2016, MNRAS, 456, 1803
Gaia Collaboration, 2018, A&A, 616, A11
Gallino R., Arlandini C., Busso M., Lugaro M., Travaglio C., Straniero O., Chieffi A., Limongi M., 1998, ApJ, 497, 388
Ghosh S., Wolfe N., Fröhlich C., 2022, ApJ, 929, 43
Gibson B. K., Fenner Y., Renda A., Kawata D., Lee H.-c., 2003, Publ. Astron. Soc. Aust., 20, 401
Goriely S., Bauswein A., Just O., Pllumbi E., Janka H. T., 2015, MNRAS, 452, 3894
Greggio L., Simonetti P., Matteucci F., 2021, MNRAS, 500, 1755
Gudin D. et al., 2021, ApJ, 908, 79
Guiglion G., de Laverny P., Recio-Blanco A., Prantzos N., 2018, A&A, 619, A143
Hansen C. J., Montes F., Arcones A., 2014, ApJ, 797, 123
Hansen T. T. et al., 2018, ApJ, 858, 92
Hansen C. J. et al., 2020, A&A, 643, A49
Haynes C. J., Kobayashi C., 2019, MNRAS, 483, 5123
Hillebrandt W., Takahashi K., Kodama T., 1976, A&A, 52, 63
Hoffman R. D., Woosley S. E., Qian Y.-Z., 1997, ApJ, 482, 951
Holmbeck E. M. et al., 2018, ApJ, 859, L24
Hotokezaka K., Beniamini P., Piran T., 2018, Int. J. Mod. Phys. D, 27, 1842005
Ivans I. I., Simmerer J., Sneden C., Lawler J. E., Cowan J. J., Gallino R., Bisterzo S., 2006, ApJ, 645, 613
Iwamoto K., Brachwitz F., Nomoto K., Kishimoto N., Umeda H., Hix W. R., Thielemann F.-K., 1999, ApJS, 125, 439
Ji A. P., Drout M. R., Hansen T. T., 2019, ApJ, 882, 40
Käppeler F., Gallino R., Bisterzo S., Aoki W., 2011, Rev. Mod. Phys., 83, 157
Karakas A. I., Lugaro M., 2016, ApJ, 825, 26
Katz D., Soubiran C., Cayrel R., Adda M., Cautain R., 1998, A&A, 338, 151
Kobayashi C., Karakas A. I., Lugaro M., 2020, ApJ, 900, 179
Kovtyukh V. V., Soubiran C., Belik S. I., Gorlova N. I., 2003, A&A, 411, 559
Kupka F., Piskunov N. E., Ryabchikova T. A., Stempels H. C., Weiss W. W., 1999, A&AS, 138, 119
Lattimer J. M., Schramm D. N., 1974, ApJ, 192, L145
Lawler J. E., Whaling W., Grevesse N., 1990, Nature, 346, 635
Limongi M., Chieffi A., 2018, ApJS, 237, 13
Mashonkina L., Christlieb N., 2014, A&A, 565, A123
Mashonkina L., Gehren T., 2001, A&A, 376, 232
Mashonkina L., Gehren T., Shi J. R., Korn A. J., Grupp F., 2011, A&A, 528, A87
Mashonkina L., Christlieb N., Eriksson K., 2014, A&A, 569, A43
Matteucci F., 2021, A&A Rev., 29, 5
Matteucci F., Romano D., Arcones A., Korobkin O., Rosswog S., 2014, MNRAS, 438, 2177
Mishenina T. V., Kovtyukh V. V., 2001, A&A, 370, 951
Mishenina T. V., Soubiran C., Kovtyukh V. V., Korotin S. A., 2004, A&A, 418, 551
Mishenina T. V., Soubiran C., Bienaymé O., Korotin S. A., Belik S. I., Usenko I. A., Kovtyukh V. V., 2008, A&A, 489, 923

Mishenina T. V., Pignatari M., Korotin S. A., Soubiran C., Charbonnel C., Thielemann F. K., Gorbaneva T. I., Basak N. Y., 2013, A&A, 552, A128
Mishenina T. et al., 2017, MNRAS, 469, 4378
Mishenina T., Pignatari M., Gorbaneva T., Bisterzo S., Travaglio C., Thielemann F. K., Soubiran C., 2019a, MNRAS, 484, 3846
Mishenina T., Pignatari M., Gorbaneva T., Travaglio C., Côté B., Thielemann F. K., Soubiran C., 2019b, MNRAS, 489, 1697
Molero M. et al., 2021, MNRAS, 505, 2913
Morell O., Kallander D., Butcher H. R., 1992, A&A, 259, 543
Mösta P., Roberts L. F., Halevi G., Ott C. D., Lippuner J., Haas R., Schnetter E., 2018, ApJ, 864, 171
Moultaka J., Ilovaisky S. A., Prugniel P., Soubiran C., 2004, PASP, 116, 693
Naiman J. P. et al., 2018, MNRAS, 477, 1206
Nilsson H., Zhang Z. G., Lundberg H., Johansson S., Nordström B., 2002, A&A, 382, 368
Ning H., Qian Y. Z., Meyer B. S., 2007, ApJ, 667, L159
Nishimura S., Kotake K., Hashimoto M.-a., Yamada S., Nishimura N., Fujimoto S., Sato K., 2006, ApJ, 642, 410
Nishimura N., Sawai H., Takiwaki T., Yamada S., Thielemann F.-K., 2017, ApJ, 836, L21
Nomoto K., Kobayashi C., Tominaga N., 2013, ARA&A, 51, 457
Obergaulinger M., Just O., Aloy M. A., 2018, J. Phys. G: Nucl. Phys., 45, 084001
Perruchot S. et al., 2008, Proc. SPIE Conf. Ser. Vol. 7014, Ground-based and Airborne Instrumentation for Astronomy II. SPIE, Bellingham, p. 70140J
Pignatari M., Gallino R., Heil M., Wiescher M., Käppeler F., Herwig F., Bisterzo S., 2010, ApJ, 710, 1557
Prantzos N., Abia C., Limongi M., Chieffi A., Cristallo S., 2018, MNRAS, 476, 3432
Prantzos N., Abia C., Cristallo S., Limongi M., Chieffi A., 2020, MNRAS, 491, 1832
Qian Y. Z., Wasserburg G. J., 2007, Phys. Rep., 442, 237
Reddy B. E., Tomkin J., Lambert D. L., Allende Prieto C., 2003, MNRAS, 340, 304
Reichert M., Obergaulinger M., Eichler M., Aloy M. Á., Arcones A., 2021, MNRAS, 501, 5733
Roederer I. U., Cowan J. J., Karakas A. I., Kratz K.-L., Lugaro M., Simmerer J., Farouqi K., Sneden C., 2010, ApJ, 724, 975
Roederer I. U., Preston G. W., Thompson I. B., Shectman S. A., Sneden C., Burley G. S., Kelson D. D., 2014, AJ, 147, 136
Rosswog S., Sollerman J., Feindt U., Goobar A., Korobkin O., Wollaeger R., Fremling C., Kasliwal M. M., 2018, A&A, 615, A132
Sakari C. M. et al., 2018, ApJ, 868, 110
Schönrich R. A., Weinberg D. H., 2019, MNRAS, 487, 580
Shchukina N., Trujillo Bueno J., 2001, ApJ, 550, 970
Siegel D. M., Barnes J., Metzger B. D., 2019, Nature, 569, 241
Simmerer J., Sneden C., Cowan J. J., Collier J., Woolf V. M., Lawler J. E., 2004, ApJ, 617, 1091
Simonetti P., Matteucci F., Greggio L., Cescutti G., 2019, MNRAS, 486, 2896
Sneden C. et al., 2003, ApJ, 591, 936
Sneden C., Cowan J. J., Gallino R., 2008, ARA&A, 46, 241
Spina L. et al., 2018, MNRAS, 474, 2580
Surman R., McLaughlin G. C., Ruffert M., Janka H.-T., Hix W. R., 2008, ApJ, 679, L117
Symbalisty E. M. D., Schramm D. N., Wilson J. R., 1985, ApJ, 291, L11
Takahashi K., Witti J., Janka H.-T., 1994, A&A, 286, 857
The L.-S., El Eid M. F., Meyer B. S., 2007, ApJ, 655, 1058
Thévenin F., Idiart T. P., 1999, ApJ, 521, 753
Thielemann F.-K., Arnould M., Hillebrandt W., 1979, A&A, 74, 175
Thielemann F.-K., Eichler M., Panov I. V., Wehmeyer B., 2017, Ann. Rev. Nucl. Part. Sci., 67, 253
Thielemann F.-K., Wehmeyer B., Wu M.-R., 2020, J. Phys. Conf. Ser., 1668, 012044
Tinsley B. M., 1980, Fundam. Cosmic Phys., 5, 287
Travaglio C., Gallino R., Arnone E., Cowan J., Jordan F., Sneden C., 2004, ApJ, 601, 864
Trueman T. C. L., Côté B., Yagüe López A., den Hartogh J., Pignatari M., Soós B., Karakas A. I., Lugaro M., 2022, ApJ, 924, 10
Truran J. W., Cowan J. J., Cameron A. G. W., 1978, ApJ, 222, L63
Tsymbal V., 1996, in Adelman S., Kupka F., Weiss W., eds, ASP Conf. Ser. Vol. 108, MASS, Model Atmospheres and Spectrum Synthesis. Astron. Soc. Pac., San Francisco, p. 198
Unterborn C. T., Johnson J. A., Panero W. R., 2015, ApJ, 806, 139
van de Voort F., Pakmor R., Grand R. J. J., Springel V., Gómez F. A., Marinacci F., 2020, MNRAS, 494, 4867
Wanajo S., Janka H.-T., Kubono S., 2011, ApJ, 729, 46
Wanajo S., Hirai Y., Prantzos N., 2021, MNRAS, 505, 5862
Wehmeyer B., Pignatari M., Thielemann F. K., 2015, MNRAS, 452, 1970
Winteler C., Käppeli R., Perego A., Arcones A., Vasset N., Nishimura N., Liebendörfer M., Thielemann F. K., 2012, ApJ, 750, L22
Woosley S. E., Wilson J. R., Mathews G. J., Hoffman R. D., Meyer B. S., 1994, ApJ, 433, 229
Yagüe López A., García-Hernández D. A., Ventura P., Doherty C. L., den Hartogh J. W., Jones S. W., Lugaro M., 2022, A&A, 657, A28
Yong D. et al., 2013, ApJ, 762, 26
Yong D. et al., 2021, Nature, 595, 223
Zenati Y., Siegel D. M., Metzger B. D., Perets H. B., 2020, MNRAS, 499, 4097

APPENDIX A:

We presented the stellar parameters and the Gd, Dy, Th abundances with errors in Table A1.

Table A1. Stellar parameters and abundances of Gd, Dy, and Th.

HD/BD thin disc	$T_{\rm eff}$, K	log g	[Fe/H]	$V_{\rm t}$	[Gd/Fe]	Standard deviation	[Dy/Fe]	Standard deviation	[Th/Fe]
166	5514	4.6	0.16	0.6	–	–	–	–	0.06
1562	5828	4.0	− 0.32	1.2	0.14	0.04	0.12	0.05	0.31
1835	5790	4.5	0.13	1.1	–	–	–	–	–
3651	5277	4.5	0.15	0.6	0.05	0.07	0.05	0.05	− 0.08
4256	5020	4.3	0.08	1.1	–	–	–	–	–
4307	5889	4.0	− 0.18	1.1	–	–	–	–	–
4614	5965	4.4	− 0.24	1.1	0.18	0.03	0.19	0.05	0.03
5294	5779	4.1	− 0.17	1.3	0.19	0.00	0.11	0.03	0.26
6660	4759	4.6	0.08	1.4	–	–	–	–	–
7590	5962	4.4	− 0.10	1.4	0.15	0.04	0.16	0.05	0.19
7924	5165	4.4	− 0.22	1.1	0.19	0.00	0.22	0.04	0.16
8648	5790	4.2	0.12	1.1	–	–	0.14	0.06	− 0.05
9407	5666	4.45	0.05	0.8	0.09	0.06	− 0.02	0.03	0.12
9826	6074	4.0	0.10	1.3	− 0.03	0.00	− 0.10	0.06	− 0.08
10086	5696	4.3	0.13	1.2	–	–	–	–	–
10307	5881	4.3	0.02	1.1	–	–	–	–	− 0.10
10476	5242	4.3	− 0.05	1.1	–	–	–	–	− 0.13
10780	5407	4.3	0.04	0.9	0.16	0.06	− 0.02	0.03	− 0.12
11007	5980	4.0	− 0.20	1.1	0.13	0.05	0.15	0.06	0.29
11373	4783	4.65	0.08	1.0	–	–	–	–	–
12846	5766	4.5	− 0.24	1.2	0.29	0.04	0.19	0.07	0.33
13507	5714	4.5	− 0.02	1.1	0.09	–	0.12	0.05	− 0.01
14374	5449	4.3	− 0.09	1.1	0.06	–	0.07	0.06	0.18
16160	4829	4.6	− 0.16	1.1	0.21	–	0.21	0.00	0.25
17674	5909	4.0	− 0.14	1.1	0.06	0.06	0.06	0.12	0.28
17925	5225	4.3	− 0.04	1.1	–	–	–	–	–
18632	5104	4.4	0.06	1.4	–	–	–	–	–
18803	5665	4.55	0.14	0.8	0.03	0.07	− 0.03	0.05	− 0.12
19019	6063	4.0	− 0.17	1.1	0.22	–	0.21	0.06	0.16
19373	5963	4.2	0.06	1.1	− 0.06	0.02	− 0.02	0.05	0.01
20630	5709	4.5	0.08	1.1	0.07	0.04	0.00	0.03	− 0.06
22049	5084	4.4	− 0.15	1.1	–	–	–	–	–
22484	6037	4.1	− 0.03	1.1	0.12	0.03	0.07	0.02	0.15
22556	6155	4.2	− 0.17	1.1	–	–	–	–	–
24053	5723	4.4	0.04	1.1	0.06	0.04	0.05	0.05	0.13
24238	4996	4.3	− 0.46	1.0	0.28	–	0.31	0.07	0.23
24496	5536	4.3	− 0.13	1.5	0.18	0.03	0.14	0.05	0.02
25665	4967	4.7	0.01	1.2	–	–	–	–	–
25680	5843	4.5	0.05	1.1	–	–	–	–	–
26923	5920	4.4	− 0.03	1.0	0.12	0.06	0.12	0.05	− 0.10
28005	5980	4.2	0.23	1.1	− 0.03	0.04	− 0.06	0.03	0.14
28447	5639	4.0	− 0.09	1.1	0.14	0.04	0.17	0.03	0.08
29150	5733	4.3	0.00	1.1	0.06	0.01	0.04	0.02	− 0.13
29310	5852	4.2	0.08	1.4	–	–	–	–	–
29645	6009	4.0	0.14	1.3	− 0.07	0.05	− 0.09	0.04	− 0.12
30495	5820	4.4	− 0.05	1.3	–	–	–		–
33632	6072	4.3	− 0.24	1.1	0.11	0.04	0.19	0.04	0.28
34411	5890	4.2	0.10	1.1	–	–	–	–	
37008	5016	4.4	− 0.41	0.8	0.18	–	0.26	–	0.18
37394	5296	4.5	0.09	1.1	–	–	–	–	–
38858	5776	4.3	− 0.23	1.1	0.19	0.09	0.18	0.07	0.12
39587	5955	4.3	− 0.03	1.5	0.11	0.03	0.05	0.03	0.20
40616	5881	4.0	− 0.22	1.1	0.17	0.04	0.15	0.03	0.16
41330	5904	4.1	− 0.18	1.2	0.15	0.05	0.19	0.06	0.32
41593	5312	4.3	− 0.04	1.1	− 0.02	0.11	0.01	0.08	− 0.14
42618	5787	4.5	− 0.07	1.0	0.11	0.03	0.17	0.05	0.01
42807	5719	4.4	− 0.03	1.1	0.09	0.08	0.06	0.05	0.05
43587	5927	4.1	− 0.11	1.3	0.01	0.06	0.07	0.05	0.30
43856	6143	4.1	− 0.19	1.1	0.19	0.04	0.09	0.04	–
43947	6001	4.3	− 0.24	1.1	0.06	0.04	0.12	0.03	0.33
45088	4959	4.3	− 0.21	1.2	0.33	0.07	0.21	0.00	0.25
47752	4613	4.6	− 0.05	0.2	–	–	–	–	− 0.13
48682	5989	4.1	0.05	1.3	− 0.08	0.09	− 0.05	0.04	0.07

Table A1 – *continued*

HD/BD thin disc	$T_{\rm eff}$, K	log g	[Fe/H]	$V_{\rm t}$	[Gd/Fe]	Standard deviation	[Dy/Fe]	Standard deviation	[Th/Fe]
50281	4712	3.9	−0.20	1.6	–	–	–	–	–
50692	5911	4.5	−0.10	0.9	0.11	0.06	0.12	0.03	0.24
51419	5746	4.1	−0.37	1.1	0.32	0.11	0.25	0.08	0.39
51866	4934	4.4	0.00	1.0	–	–	–	–	–
53927	4860	4.64	−0.22	1.2	0.17	0.04	0.27	0.00	0.11
54371	5670	4.2	0.06	1.2	–	–	–	–	–
55575	5949	4.3	−0.31	1.1	0.18	0.04	0.21	0.06	0.35
58595	5707	4.3	−0.31	1.2	0.20	0.08	0.21	0.04	0.30
59747	5126	4.4	−0.04	1.1	−0.04	0.07	−0.01	–	−0.04
61606	4956	4.4	−0.12	1.3	–	–	–	–	–
62613	5541	4.4	−0.10	1.1	0.14	0.08	0.11	0.08	0.14
63433	5693	4.35	−0.06	1.9	0.08	0.00	0.23	0.03	0.15
64468	5014	4.2	0.00	1.2	0.07	0.00	−0.02	0.06	−0.13
64815	5864	4.0	−0.33	1.1	0.28	0.08	0.23	0.08	–
65874	5936	4.0	0.05	1.3	–	–	–	–	–
66573	5821	4.6	−0.53	1.1	0.38	0.06	0.37	0.05	0.45
68638	5430	4.4	−0.24	1.1	0.14	0.06	0.09	0.05	0.23
70923	5986	4.2	0.06	1.1	0.00	0.05	−0.07	0.05	0.06
71148	5850	4.2	0.00	1.1	–	–	–	–	−0.13
72760	5349	4.1	0.01	1.1	–	–	–	–	–
72905	5884	4.4	−0.07	1.5	–	–	–	–	–
73344	6060	4.1	0.08	1.1	0.02	0.04	−0.11	0.05	−0.06
73667	4884	4.4	−0.58	0.9	0.42	0.06	0.28	0.05	0.55
75732	5373	4.3	0.25	1.1	−0.07	0.04	−0.13	0.06	0.02
75767	5823	4.2	−0.01	0.9	–	–	–	–	–
76151	5776	4.4	0.05	1.1	–	–	–	–	–
79969	4825	4.4	−0.05	1.0	–	–	–	–	–
82106	4827	4.1	−0.11	1.1	0.08	0.07	0.04	0.04	0.25
82443	5334	4.4	−0.03	1.3	−0.03	0.08	0.10	0.03	0.10
87883	5015	4.4	0.00	1.1	–	–	–	–	–
88072	5778	4.3	0.00	1.1	0.05	0.03	0.07	0.03	0.02
89251	5886	4.0	−0.12	1.1	–	–	0.14	0.08	–
89269	5674	4.4	−0.23	1.1	0.19	0.05	0.09	0.05	0.17
91347	5931	4.4	−0.43	1.1	0.24	0.05	0.26	0.03	0.50
94765	5077	4.4	−0.01	1.1	0.15	0.06	0.01	0.04	−0.07
95128	5887	4.3	0.01	1.1	0.06	0.00	0.02	0.03	0.01
97334	5869	4.4	0.06	1.2	−0.02	0.04	−0.04	0.03	0.06
97658	5136	4.5	−0.32	1.2	0.29	0.07	0.27	0.04	0.21
98630	6060	4.1	0.22	1.4	–	–	–	–	–
101177	5932	4.1	−0.16	1.1	0.13	0.07	0.14	0.03	0.25
102870	6055	4.0	0.13	1.4	−0.09	0.05	−0.04	0.05	0.09
105631	5416	4.4	0.16	1.2	–	–	–	–	–
107705	6040	4.2	0.06	1.4	–	–	–	–	–
108954	6037	4.4	−0.12	1.1	–	–	–	–	0.21
109358	5897	4.2	−0.18	1.1	0.14	0.05	0.12	0.03	0.32
110463	4950	4.5	−0.05	1.2	–	–	–	–	–
110833	5075	4.3	0.00	1.1	–	–	–	–	–
111395	5648	4.6	0.10	0.9	0.02	0.09	−0.05	0.00	–
112758	5203	4.2	−0.56	1.1	–		–	–	–
114710	5954	4.3	0.07	1.1	−0.05	0.04	−0.03	0.05	−0.05
115383	6012	4.3	0.11	1.1	−0.06	0.03	0.01	0.03	0.01
115675	4745	4.45	0.02	1.0	–	–	–	–	–
116443	4976	3.9	−0.48	1.1	–	–	–	–	0.35
116956	5386	4.55	0.08	1.2	0.06	0.06	−0.01	0.03	−0.21
117043	5610	4.5	0.21	0.4	−0.02	0.03	−0.14	0.03	−0.09
119802	4763	4.0	−0.05	1.1	–	–	–	–	–
122064	4937	4.5	0.07	1.1	–	–	–	–	−0.05
124642	4722	4.65	0.02	1.3	–	–	–	–	–
125184	5695	4.3	0.31	0.7	–	–	–	–	–
126053	5728	4.2	−0.32	1.1	0.19	0.05	0.16	0.05	0.46
127506	4542	4.6	−0.08	1.2	–	–	–	–	–
128311	4960	4.4	0.03	1.3	0.16	0.05	0.00	0.03	–
130307	4990	4.3	−0.25	1.4	0.27	0.05	0.23	0.03	–

Table A1 *– continued*

HD/BD thin disc	$T_{\rm eff}$, K	log g	[Fe/H]	$V_{\rm t}$	[Gd/Fe]	Standard deviation	[Dy/Fe]	Standard deviation	[Th/Fe]
130948	5943	4.4	− 0.05	1.3	–	–	–	–	–
131977	4683	3.7	− 0.24	1.8	–	–	–	–	–
135599	5257	4.3	− 0.12	1.0	0.07	0.04	0.11	0.05	0.21
137107	6037	4.3	0.00	1.1	0.05	0.03	0.05	0.04	− 0.13
139777	5771	4.4	0.01	1.3	0.11	0.00	0.08	0.05	–
139813	5408	4.5	0.00	1.2	–	–	–	–	–
140538	5675	4.5	0.02	0.9	–	–	–	–	–
141004	5884	4.1	− 0.02	1.1	0.12	0.03	0.08	0.06	0.04
141272	5311	4.4	− 0.06	1.3	0.16	0.03	0.09	0.03	0.00
142267	5856	4.5	− 0.37	1.1	–	–	–	–	–
144287	5414	4.5	− 0.15	1.1	0.22	0.05	0.21	0.03	0.19
145675	5406	4.5	0.32	1.1	− 0.05	0.05	− 0.10	0.03	0.10
146233	5799	4.4	0.01	1.1	0.14	0.03	0.13	0.02	− 0.09
149661	5294	4.5	− 0.04	1.1	0.16	0.07	0.09	0.05	− 0.14
149806	5352	4.55	0.25	0.4	–	–	–	–	–
151541	5368	4.2	− 0.22	1.3	–	–	–	–	–
153525	4810	4.7	− 0.04	1.0	–	–	–	–	–
154345	5503	4.3	− 0.21	1.3	0.18	0.05	0.11	0.04	0.35
156668	4850	4.2	− 0.07	1.2	0.17	0.04	0.22	0.07	0.16
156985	4790	4.6	− 0.18	1.0	–		–		0.17
158633	5290	4.2	− 0.49	1.3	0.20	0.08	0.19	0.04	0.51
160346	4983	4.3	− 0.10	1.1	–	–	–	–	–
161098	5617	4.3	− 0.27	1.1	–	–	–	–	–
164922	5392	4.3	0.04	1.1	–	–	–	–	–
165173	5505	4.3	− 0.05	1.1	0.15	0.06	0.09	–	− 0.03
165341	5314	4.3	− 0.08	1.1	–	–	–	–	− 0.03
165476	5845	4.1	− 0.06	1.1	–	–	–	–	–
165670	6178	4.0	− 0.10	1.5	–	–	–	–	–
165908	5925	4.1	− 0.60	1.1	0.25	0.04	0.30	0.06	–0.37
166620	5035	4.0	− 0.22	1.0	–	–	–	–	–
171314	4608	4.65	0.07	1.0	–	–	–	–	–
174080	4764	4.55	0.04	1.0	–	–	–	–	0.08
175742	5030	4.5	− 0.03	2.0	–	–	–	–	–
176377	5901	4.4	− 0.17	1.3	0.14	0.07	0.18	0.02	0.11
176841	5841	4.3	0.23	1.1	–	–	–	–	− 0.11
178428	5695	4.4	0.14	1.0	–	–	–	–	− 0.17
180161	5473	4.5	0.18	1.1	–	–	–	–	–
182488	5435	4.4	0.07	1.1	–	–	–	–	0.05
183341	5911	4.3	− 0.01	1.3	–	–	–	–	–
184385	5536	4.45	0.12	0.9	0.00	0.05	− 0.03	0.05	–
185144	5271	4.2	− 0.33	1.1	0.10	0.05	0.06	0.03	0.37
185414	5818	4.3	− 0.04	1.1	0.04	0.04	0.08	0.02	− 0.14
186408	5803	4.2	0.09	1.1	–	–	–	–	− 0.22
186427	5752	4.2	0.02	1.1	–	–	–	–	− 0.10
187897	5887	4.3	0.08	1.1	− 0.01	0.05	− 0.02	0.06	− 0.01
189087	5341	4.4	− 0.12	1.1	–	–	–	–	0.01
189733	5076	4.4	− 0.03	1.5	0.13	0.04	0.13	0.05	–
190007	4724	4.5	0.16	0.8	–	–	–	–	–
190406	5905	4.3	0.05	1.0	–	–	–	–	0.07
190470	5130	4.3	0.11	1.0	0.00	0.06	− 0.10	0.05	− 0.14
190771	5766	4.3	0.13	1.5	–	–	–	–	–
191533	6167	3.8	− 0.10	1.5	–	–	–	–	0.19
191785	5205	4.2	− 0.12	1.2	0.12	0.04	0.08	0.06	0.26
195005	6075	4.2	− 0.06	1.3	–	–	–	–	0.08
195104	6103	4.3	− 0.19	1.1	–	–	–	–	–
197076	5821	4.3	− 0.17	1.2	0.09	0.05	0.11	0.05	0.29
199960	5878	4.2	0.23	1.1	–	–	–	–	–
200560	5039	4.4	0.06	1.1	–	–	–	–	–
202108	5712	4.2	− 0.21	1.1	0.16	0.08	0.19	0.03	0.35
202575	4667	4.6	− 0.03	0.5	–	–	–	–	0.20
203235	6071	4.1	0.05	1.3	–	–	–	–	–
205702	6020	4.2	0.01	1.1	0.06	0.07	− 0.01	0.05	0.21

Table A1 – *continued*

HD/BD thin disc	$T_{\rm eff}$, K	log g	[Fe/H]	$V_{\rm t}$	[Gd/Fe]	Standard deviation	[Dy/Fe]	Standard deviation	[Th/Fe]
206860	5927	4.6	−0.07	1.8	0.09	0.07	0.10	–	0.16
208038	4982	4.4	−0.08	1.0	–	–	–	–	–
208313	5055	4.3	−0.05	1.0	–	–	–	–	–
208906	5965	4.2	−0.80	1.7	0.44	0.13	0.39	0.05	0.57
210667	5461	4.5	0.15	0.9	0.12	0.05	0.03	0.03	–
210752	6014	4.6	−0.53	1.1	0.40		0.41	0.04	–
211472	5319	4.4	−0.04	1.1	0.04	0.03	0.06	0.03	0.06
214683	4747	4.6	−0.46	1.2	–	–	–	–	0.53
216259	4833	4.6	−0.55	0.5	–	–	–	–	–
216520	5119	4.4	−0.17	1.4	–	–	–	–	–
217014	5763	4.3	0.17	1.1	−0.08	0.08	0.02	0.05	−0.10
217813	5845	4.3	0.03	1.5	0.04	0.00	0.02	0.00	–
218868	5547	4.45	0.21	0.4	–	–	–	–	−0.19
219538	5078	4.5	−0.04	1.1	–	–	–	–	–
219623	5949	4.2	0.04	1.2	–	–	–	–	−0.12
220140	5144	4.6	−0.03	2.4	–	–	–	–	–
220182	5364	4.5	−0.03	1.2	–	–	–	–	–
220221	4868	4.5	0.16	0.5	0.09	0.04	0.06	0.03	−0.04
221851	5184	4.4	−0.09	1.0	0.16	0.07	0.12	0.03	–
222143	5823	4.45	0.15	1.1	–	–	–	–	–
224465	5745	4.5	0.08	0.8	–	–	–	–	–
263175	4734	4.5	−0.16	0.5	0.16	0.03	0.14	0.04	0.13
BD12063	4859	4.4	−0.22	0.6	0.19	0.00	0.21	0.05	0.34
BD124499	4678	4.7	0.00	0.5	–	–	–	–	–
thick disc									
245	5400	3.4	−0.84	0.7	0.38	0.12	0.47	0.05	0.46
3765	5079	4.3	0.01	1.1	0.06	0.07	0.07	0.05	−0.01
5351	4378	4.6	−0.21	0.5	–	–	–	–	0.33
6582	5350	4.5	−0.83	0.4	0.28	0.06	0.22	0.06	0.60
13783	5350	4.1	−0.75	1.1	–	–	–	–	0.57
18757	5741	4.3	−0.25	1.0	0.15	0.03	0.16	0.05	0.32
22879	5825	4.42	−0.91	0.9	0.41	0.03	0.38	0.03	0.58
65583	5373	4.6	−0.67	0.7	0.37	0.06	0.34	0.08	0.49
76932	5840	4.0	−0.95	1.0	–	–	–	–	0.57
106516	6165	4.4	−0.72	1.1	–	–	–	–	–
110897	5925	4.2	−0.45	1.1	0.15	0.06	0.16	0.05	0.42
135204	5413	4.0	−0.16	1.1	–	–	–		0.03
152391	5495	4.3	−0.08	1.3	0.13	0.06	0.07	0.05	0.10
157089	5785	4.0	−0.56	1.0	–	–	–	–	0.43
157214	5820	4.5	−0.29	1.0	–	–	–	–	0.21
159062	5414	4.3	−0.40	1.0	0.34	0.03	0.23	0.05	0.27
165401	5877	4.3	−0.36	1.1	–	–	–	–	0.13
190360	5606	4.4	0.12	1.1	−0.02	0.03	0.04	–	0.15
201889	5600	4.1	−0.85	1.2	0.40	0.03	0.41	0.05	0.57
201891	5850	4.4	−0.96	1.0	0.45	0.03	0.37	0.03	0.58
204521	5809	4.6	−0.66	1.1	0.40	0.03	0.36	0.05	0.58
Hercules stream									
13403	5724	4.0	−0.31	1.1	0.20	0.03	0.19	0.05	0.48
19308	5844	4.3	0.08	1.1	−0.03	0.03	−0.04	0.02	0.14
23050	5929	4.4	−0.36	1.1	0.23	0.07	0.22	0.02	0.43
30562	5859	4.0	0.18	1.1	–	–	–	–	–
64606	5250	4.2	−0.91	0.8	0.33	0.05	0.35	0.05	0.73
68017	5651	4.2	−0.42	1.1	–	–	–	–	–
81809	5782	4	−0.28	1.3	0.18	0.03	0.15	0.03	0.25
107213	6156	4.1	0.07	1.6	−0.05	0.07	−0.10	0.04	0.15
139323	5204	4.6	0.19	0.7	−0.09	0.06	0.04	0.03	−0.02
139341	5242	4.6	0.21	0.9	–	–	–	–	–
144579	5294	4.1	−0.70	1.3	0.35	0.03	0.35	0.04	0.67
159222	5834	4.3	0.06	1.2	0.01	0.05	0.00	0.06	−0.04
159909	5749	4.1	0.06	1.1	–	–	–	–	–
215704	5418	4.2	0.07	1.1	–	–	–	–	–
218209	5705	4.5	−0.43	1.0	0.32	0.03	0.32	0.05	0.50
221354	5242	4.1	−0.06	1.2	0.06		0.09		0.08

Table A1 *– continued*

HD/BD thin disc	$T_{\rm eff}$, K	log g	[Fe/H]	$V_{\rm t}$	[Gd/Fe]	Standard deviation	[Dy/Fe]	Standard deviation	[Th/Fe]
Non-classified									
4628	4905	4.6	− 0.36	0.5	–	–	0.24	0.05	–
4635	5103	4.4	0.07	0.8	0.05	0.10	0.11	0.10	0.15
10145	5673	4.4	− 0.01	1.1	–	–	–	–	–
12051	5458	4.55	0.24	0.5	–	–	–	–	–
13974	5590	3.8	− 0.49	1.1	0.14	0.03	0.07	0.03	0.31
17660	4713	4.75	0.17	1.3	–	–	–	–	–
20165	5145	4.4	− 0.08	1.1	–	–	–	–	–
24206	5633	4.5	− 0.08	1.1	0.10	0.00	0.12	0.05	0.20
32147	4945	4.4	0.13	1.1	0.02	0.04	− 0.01	0.03	0.29
45067	6058	4.0	− 0.02	1.2	–	–	–	–	–
84035	4808	4.8	0.25	0.5	–	–	–	–	–
86728	5725	4.3	0.22	0.9	–	–	–	–	–
90875	4788	4.5	0.24	0.5	–	–	–	–	–
117176	5611	4.0	− 0.03	1.0	0.10	0.05	0.11	0.03	0.25
117635	5230	4.3	− 0.46	0.7	–	–	–	–	–
154931	5910	4.0	− 0.10	1.1	–	–	–	–	–
159482	5620	4.1	− 0.89	1.0	–	–	–	–	–
168009	5826	4.1	− 0.01	1.1	–	–	–	–	–
173701	5423	4.4	0.18	1.1	− 0.01	0.07	− 0.02	0.05	0.14
182736	5430	3.7	− 0.06	1.0	0.10	0.03	0.11	0.04	0.23
184499	5750	4.0	− 0.64	1.5	0.31	0.00	0.33	0.03	0.66
184768	5713	4.2	− 0.07	1.1	–	–	–	–	–
186104	5753	4.2	0.05	1.1	–	–	–	–	–
215065	5726	4.0	− 0.43	1.1	0.27	0.03	0.18	0.04	0.35
219134	4900	4.2	0.05	0.8	–	–	–	–	–
219396	5733	4.0	− 0.10	1.2	0.09	0.03	0.15	0.05	0.32
224930	5300	4.1	− 0.91	0.7	0.33	0.05	0.20	0.02	0.61

This paper has been typeset from a TEX/LATEX file prepared by the author.